RSC Advances

ROYAL SOCIETY OF CHEMISTRY

PAPER

View Article Online
View Journal | View Issue

Check for updates

Cite this: *RSC Adv.*, 2026, **16**, 13559

Supercritical catalytic cracking of *n*-decane over microwave-synthesized hierarchical core–shell nano-Beta@SBA-15 composite zeolite

Hailong Ma,[a] Hui Gao,*[a] Jieyin Ma,[a] Jiajun Zhao,[a] Chen Zhang[b] and Dongsheng Wen[ac]

Received 31st December 2025
Accepted 5th March 2026

DOI: 10.1039/d5ra10130a

rsc.li/rsc-advances

Catalytic cracking of endothermic hydrocarbon fuels offers a promising regenerative cooling strategy for hypersonic propulsion systems, yet conventional microporous zeolite catalysts suffer from severe diffusion limitations and rapid coke deposition under supercritical conditions. This study develops a hierarchical core–shell Beta@SBA-15 composite zeolite *via* a microwave synthesis method, integrating microporous nano zeolite Beta as the catalytic core with ordered mesoporous SBA-15 as the transport shell. Comprehensive characterization confirms the core–shell structure and the intimate integration of both components. Such core–shell catalyst exhibits 14.9% higher acidity-normalized activity than nano zeolite Beta. Its exceptional enhanced stability and reduced coke formation were also demonstrated, with only 25.39% conversion loss over 15 hour time-on-stream tests compared to 47.45% for nano zeolite Beta, while substantially reducing coke deposition from 6.3% to 3.8%. These results are attributed to the core–shell structure, where the mesoporous shell improves active site accessibility, facilitates rapid product and coke precursor removal, and effectively mitigates diffusion limitations in catalytic processes. These findings reveal the structure–performance correlation of microporous core-ordered mesoporous shell zeolite catalysts, offering insights for hydrocarbon conversion under extreme conditions.

1. Introduction

The development of hypersonic scramjet propulsion systems is critically constrained by unprecedented thermal loads that exceed conventional cooling capacities.[1–3] Regenerative cooling utilizing onboard endothermic hydrocarbon fuels (EHF) has emerged as a promising strategy, exploiting both physical and chemical heat sinks to dissipate thermal loads and protect propulsion systems.[4–6] However, practical implementation faces significant challenges including insufficient heat sink capacity, inadequate heat transfer efficiency, and severe coke deposition.[7] Catalytic cracking offers a promising solution by modulating cracking pathways, managing product distributions, and controlling reaction kinetics to enhance heat absorption while simultaneously mitigating coking issues.[8,9] Consequently, developing high-performance catalysts capable of enhancing endothermic capacity and suppressing coke formation has become a critical research priority, particularly under practical constraints of high fuel flow rates and limited residence time in cooling channels.[10,11]

Among various catalytic materials, zeolites have attracted considerable attention for hydrocarbon conversion due to their well-defined microporous structures, tunable acidity, and superior hydrothermal stability.[12,13] Their uniform pore dimensions and shape-selective properties enable controlled reaction pathways, while adjustable acid site characteristics optimize cracking activity and product selectivity.[14,15] However, conventional microporous zeolites face significant challenges in long-chain hydrocarbon cracking applications. The exclusive microporous structure, despite enabling high catalytic activity, creates extended diffusion pathways that compromise mass transfer efficiency. Moreover, coke precursors generated during cracking may undergo secondary reactions within confined micropores, forming carbonaceous deposits that ultimately block channels and cause catalyst deactivation. These limitations necessitate the development of hierarchical zeolites with integrated mesopores to significantly reduce diffusion resistance.[16,17]

The hierarchical architecture introduces secondary mesoporous transport pathways that enhance active site accessibility, facilitate product and coke precursor removal, and simultaneously improve mass transfer efficiency while maintaining catalytic performance.[18,19] These structural benefits have proven particularly valuable in hydrocarbon cracking, where optimized micropore–mesopore integration balances reactant diffusion with cracking depth, enabling efficient conversion of bulky long-chain hydrocarbons while suppressing deactivation.[20,21]

---

[a] School of Aeronautic Science and Engineering, Beihang University, Beijing, 100191, China. E-mail: h.gao@buaa.edu.cn

[b] Hangzhou International Innovation Institute, Beihang University, China

[c] Institute of Thermodynamics, Technical University of Munich, Munich, Germany

Most critically for regenerative cooling applications, hierarchical structures exhibit substantially lower deactivation rates than conventional microporous materials during supercritical hydrocarbon cracking, attributed to enhanced mass transfer that effectively mitigates coke accumulation.[22,23] Our previous work demonstrated that hierarchical nano-sized zeolite Beta with balanced acidity effectively mitigated diffusion limitations during high-pressure catalytic processes, achieving enhanced catalytic performance and superior coke resistance.[24]

However, these hierarchical zeolites typically possess randomly distributed mesopores that, despite improving mass transfer, still suffer from tortuous diffusion pathways and non-uniform pore accessibility that limit catalytic efficiency. In contrast, architectures with ordered mesoporous structures demonstrate superior performance by providing well-defined geometry that creates uniform diffusion pathways, minimizes transport resistance, and ensures consistent active site accessibility.[25,26] Studies on FAU and Beta zeolites with ordered 2D-hexagonal or 3D-cubic mesoporous architectures confirm that such structural precision effectively mitigates diffusion limitations, optimizes reactant-product transport, and substantially reduces internal coke formation.[27,28] Among ordered mesoporous configurations, core–shell architectures represent a particularly elegant design that spatially segregates catalytic and transport functions within a unified framework. The microporous zeolite core concentrates strong acid sites for rapid cracking reactions, while the ordered mesoporous shell provides molecular highways for efficient reactant delivery and product evacuation, creating synergistic effects unattainable in conventional structures.[29,30] Core–shell composites such as FAU/SBA-15 and HZSM-5@MCM-41 demonstrate effective functional compartmentalization in hydrocarbon conversion, with a mesoporous shell serving as a pre-cracking zone and enhancing molecular accessibility to the acidic core while facilitating product and coke precursor removal. This results in improved product selectivity and substantially mitigates catalyst deactivation.[31,32] Despite the promising results, there are still critical knowledge gaps concerning how core–shell architectures affect mass transfer dynamics, catalytic stability, and coking resistance in supercritical hydrocarbon cracking. This understanding is crucial for the rational design of catalysts in regenerative cooling applications.

Herein, this study developed a Beta@SBA-15 core–shell catalyst and systematically evaluated its performance in supercritical *n*-decane cracking for regenerative cooling applications. The core–shell architecture integrates nano zeolite Beta's catalytic activity with SBA-15's ordered mesoporous structure to enhance mass transfer and suppress coke deposition. Systematic characterization elucidated the structural, textural, and acidic properties of the material. Catalytic performance was comprehensively evaluated through supercritical *n*-decane cracking, focusing on conversion, product selectivity, and long-term stability. Results demonstrated that the core–shell architecture significantly improved mass transfer efficiency, enhanced catalytic stability, and markedly increased coking resistance during supercritical cracking. Compared to the parent zeolite Beta, the core–shell catalyst exhibits substantially reduced coke formation and extended catalytic retention, while maintaining comparable cracking activity. These findings provide critical insights into rational design principles for hierarchical zeolite catalysts with ordered mesoporous structure in hydrocarbon applications under extreme conditions.

2. Experimental section

2.1. Materials

Tetraethyl orthosilicate (TEOS), sodium aluminate ($NaAlO_2$) and magnesium sulfate anhydrous ($MgSO_4$) were purchased from InnoChem Science & Technology Co., Ltd. Tetraethylammonium hydroxide (TEAOH, 25 wt%) was supplied by J&K Scientific Ltd. Polyvinylpyrrolidone (PVP, average $M_n \sim 58\,000$) and Pluronic P123 ($EO_{20}PO_{70}EO_{20}$, average $M_n \sim 5800$) were obtained from Macklin Biochemical Technology Co., Ltd. Hydrochloric acid (HCl, 37%) was purchased from Lanyi Chemical Co., Ltd. All reagents were used without further purification.

2.2. Catalyst preparation

Nano zeolite Beta was synthesized *via* a microwave crystallization method assisted with the surfactant, following a procedure described in a previous study.[24] In a typical synthesis, TEOS was used as the silicon source, $NaAlO_2$ as the aluminum source, and TEAOH as the structure directing agent. PVP was employed to modify crystal growth and achieve nanoscale particle size. The synthesis gel was subjected to microwave heating at 180 °C for 3 h, followed by centrifugation, washing with deionized water to neutral pH, and drying overnight at 80 °C. The dried sample was calcined at 600 °C for 5 h to remove organic templates and impurities, producing the sample designated as Beta.

SBA-15 was synthesized using P123 as the structure-directing agent under microwave conditions. P123 (1.0 g) was dissolved in a mixture of 5.25 mL hydrochloric acid (37%) and 26.3 mL deionized water at 45 °C with constant stirring. Tetraethyl orthosilicate (2.14 g) was subsequently added dropwise, and the mixture was vigorously stirred at 55 °C for 5 min. The resulting gel was transferred to a Teflon-lined autoclave and subjected to microwave heating at 55 °C for 3 h, followed by crystallization at 100 °C for 3 h. The solid product was recovered by centrifugation, washed with deionized water, dried at 80 °C overnight, and calcined at 600 °C for 5 h to remove the organic template. The sample was designated as SBA-15.

Beta@SBA-15 core–shell composites were synthesized by incorporating pre-synthesized nano-Beta zeolite into the SBA-15 synthesis system. P123 (0.5 g) was dissolved in a mixture of 2.6 mL HCl (37%) and 52.6 mL deionized water at 50 °C and stirred for 1 h. After complete dissolution, 1.0 g of $MgSO_4$ was added and stirred for another hour to enhance the interaction between inorganic and organic species, facilitating the regular coating of ordered mesoporous silica on the zeolite surface.[30] Beta zeolite (1.0 g) was dispersed in the solution under ultrasonication for 30 min. TEOS (1.0 g) was added dropwise, and the mixture was vigorously stirred at 55 °C for 5 minutes. The gel was then transferred to a Teflon-lined autoclave and subjected to microwave heating at 55 °C for 3 h, followed by crystallization at 100 °C for 3 h. Solid products were recovered and post-treated, yielding samples denoted as Beta@SBA-15. In comparison, a physical mixture of Beta and SBA-15 with a mass ratio of 1 : 1 was prepared and designated as Beta/SBA-15.

2.3. Catalyst characterization

The crystalline phase and structure of the synthesized materials were characterized by powder X-ray diffraction (XRD) using Cu Kα radiation. Small-angle XRD patterns were collected in the 2θ range of 0.5–5° to identify the ordered mesoporous structure of SBA-15, while wide-angle patterns were recorded from 5–50° to analyze the *BEA zeolite framework crystallinity. Scanning electron microscopy (SEM) and transmission electron microscopy (TEM) were employed to examine morphological features, particle size distribution, and crystal structures. Energy-dispersive X-ray spectroscopy (EDX) was performed with SEM analysis to determine elemental composition and confirm the silicon-to-aluminum ratio of the synthesized materials. Textural properties were characterized by nitrogen adsorption–desorption isotherms at 77 K. Specific surface areas were determined using the Brunauer–Emmett–Teller (BET) method, and pore size distributions were analyzed *via* the Barrett–Joyner–Halenda (BJH) method applied to the desorption branch. Catalyst acidity was assessed through ammonia temperature-programmed desorption (NH_3-TPD) to quantify both weak and strong acid sites. The samples were pre-treated under helium flow at 300 °C for 1 hour, then cooled to 50 °C and exposed to a 10% NH_3/He mixture (30 mL min^{-1}) for 1 hour to achieve complete saturation. Physisorbed ammonia was removed by purging with helium for 1 hour. The temperature-programmed desorption was then performed by heating from 50 °C to 600 °C at a controlled rate of 10 °C min^{-1} while monitoring NH_3 desorption with a thermal conductivity detector. Thermogravimetric analysis (TGA) was performed under air atmosphere to examine the thermal stability of fresh catalysts and determine coke content of spent catalysts after reaction.

2.4. Catalytic activity evaluation

Catalytic performance was evaluated by catalytic cracking of *n*-decane using a high-pressure fixed-bed reactor under supercritical conditions, as shown in Fig. 1. Experiments employed 0.5 g of catalyst in a stainless-steel reactor tube, with nitrogen carrier gas maintained at 50 mL min^{-1} and *n*-decane feedstock delivered at 0.2 mL min^{-1}. Reactions were conducted at 3.5 MPa under different temperatures, with a fixed weight hourly space velocity of 17.64 h^{-1}. After a 30 min stabilization period, the effluent stream was cooled and phase-separated. Gas-phase products were analyzed using a Shimadzu GC-2014C with flame ionization and thermal conductivity detectors, while liquid-phase components were examined by PerkinElmer 2400GCMS gas chromatography-mass spectrometry.

The catalytic performance was evaluated by *n*-decane conversion rate $X_{C_{10}H_{22}}$ and selectivity to specific product S_{C_i}, as represented by eqn (1) and (2).

$$X_{C_{10}H_{22}}\ (\%) = \frac{F_{C_{10}H_{22},in} - F_{C_{10}H_{22},out}}{F_{C_{10}H_{22},in}} \times 100\% \tag{1}$$

$$S_{C_i}\ (\%) = \frac{Y_i}{\sum\limits_{products} Y_i} \times 100\% \tag{2}$$

where $F_{C_{10}H_{22},in}$ and $F_{C_{10}H_{22},out}$ are the molar flow rates of *n*-decane at the reactor inlet and outlet, respectively, and Y_i is the yield of product *i*.

3. Results and discussion

3.1. Structural and physicochemical characterization

XRD patterns of the synthesized materials reveal distinct structural characteristics. In the low-angle region, the characteristic diffraction peak at 0.9° for SBA-15, Beta/SBA-15, and Beta@SBA-15 samples corresponds to the hexagonal mesoporous SBA-15 structure. Notably, Beta@SBA-15 exhibits a well-resolved shoulder peak at approximately 1.5°, with intensity comparable to pristine SBA-15, confirming that the SBA-15 framework remains highly ordered despite the encapsulation process. In the wide-angle region, Beta, Beta/SBA-15, and Beta@SBA-15 samples display diffraction peaks at 7.5°, 21.4°, 22.4°, and 43.5°, consistent with the *BEA zeolite framework topology. In contrast, pure SBA-15 shows a broad diffraction hump in the 20–30° range, characteristic of amorphous silica walls. The coexistence of SBA-15 mesoporous features and Beta

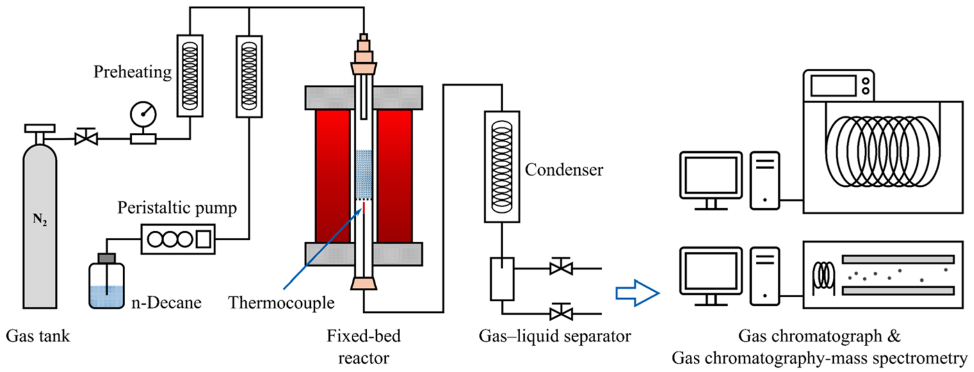

Fig. 1 Experimental setup for catalytic cracking of *n*-decane under supercritical conditions.

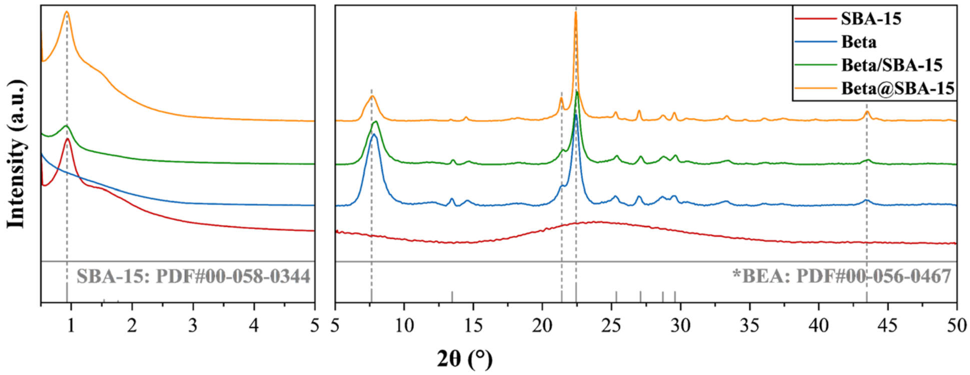

Fig. 2 XRD patterns of SBA-15, Beta, Beta/SBA-15, and Beta@SBA-15 samples in low-angle (0.5–5°) and wide-angle (5–50°) ranges.

zeolite crystalline phases in the Beta@SBA-15 sample confirms the successful synthesis of a hierarchical composite material combining ordered mesoporous SBA-15 with the microporous crystalline Beta zeolite framework (Fig. 2).

The morphological characteristics of the synthesized materials were investigated by SEM and TEM, as depicted in Fig. 3. For the physically mixed Beta/SBA-15 reference, SEM/TEM analysis reveals no distinct features beyond those of the parent materials. Therefore, the discussion focuses on SBA-15, Beta, and the designed core–shell Beta@SBA-15 sample. SEM imaging revealed distinct morphological features for each sample. The Beta zeolite (Fig. 3b) exhibited particulate morphology with particles measuring approximately 100 nm, whereas SBA-15 (Fig. 3a) displayed spherical particles with diameters of approximately 1 μm. Notably, the Beta@SBA-15 core–shell composite (Fig. 3c) maintained a similar particle size to the Beta sample while demonstrating clearly defined mesoporous surface features, indicating successful encapsulation of Beta nanoparticles within the SBA-15 shell structure. TEM analysis provides further insight into the internal structure of these materials. The Beta zeolite (Fig. 3e) exhibits well-defined lattice fringes, indicating high crystallinity consistent with XRD analysis. In contrast, SBA-15 (Fig. 3d) displays regular alternating regions corresponding to ordered mesoporous channels with approximately 10 nm spacing, characteristic of its mesoporous structure. The Beta@SBA-15 composite (Fig. 3f) demonstrates the coexistence of both structural features: distinct lattice fringes of the Beta zeolite framework are observed in the core region, while ordered mesoporous structures are visible around the particle periphery. This morphological evidence confirms the successful construction of

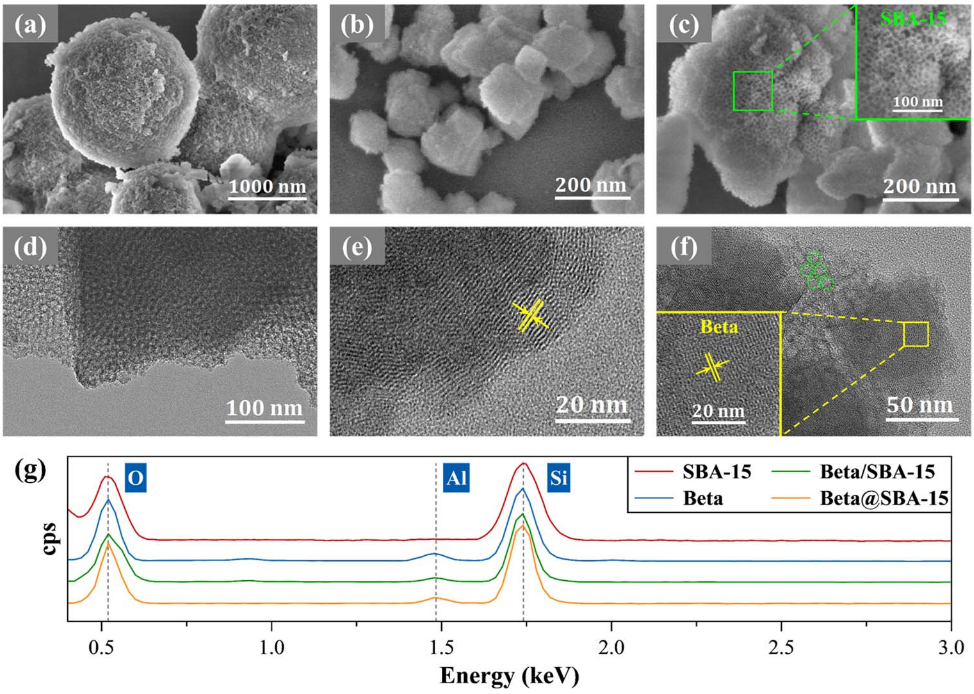

Fig. 3 SEM and TEM images of SBA-15 (a and d), Beta (b and e), and Beta@SBA-15 (c and f) samples, and EDX of synthesized zeolites (g).

Table 1 Textural properties and acid site amounts of synthesized zeolites

		Surface area (m^2 g^{-1})			Pore volume (cm^3 g^{-1})			Acid density ($mmol$ g^{-1})		
Catalyst	Si : Al	S_{BET}	S_{micro}	S_{ext}	V_{total}	V_{micro}	V_{meso}	A_L	A_H	Total acidity A_c (mmol g^{-1})
SBA-15	∞	688	159	529	0.649	0.062	0.587	0.615	0.322	0.937
Beta	20.65	610	579	31	0.278	0.232	0.046	1.086	0.451	1.537
Beta/SBA-15	47.19	647	401	246	0.446	0.166	0.280	0.784	0.309	1.093
Beta@SBA-15	32.24	736	551	185	0.452	0.227	0.225	0.817	0.366	1.183

a hierarchical core–shell architecture with Beta nanocrystals effectively encapsulated within the SBA-15 framework.

Energy-dispersive X-ray spectroscopy (EDX) was used to determine the Si/Al ratios of the calcined catalysts. The results are presented in Fig. 3g and Table 1, confirming the successful preparation of materials with distinct aluminum distributions. Beta zeolite has a Si/Al ratio of 20.65, consistent with its synthesis conditions and strong acidity. SBA-15 exhibits an infinite Si/Al ratio, confirming its purely siliceous nature as expected. The mechanical mixture Beta/SBA-15 shows a Si/Al ratio of 47.19, significantly higher than pure Beta zeolite due to the dilution effect of aluminum-free SBA-15. Beta@SBA-15 has a lower Si/Al ratio of 32.24 compared to the mechanical mixture, indicating a relatively thin SBA-15 shell encapsulating the Beta core. This core–shell structure maintains the Beta core as the dominant contributor to the overall composition, successfully achieving a controlled shell thickness that exposes the active sites of the Beta component while creating the desired hierarchical pore structure.

The textural properties of the catalysts were characterized by N_2 physisorption, as depicted in Fig. 4 and Table 1. The isotherms reveal distinct adsorption behaviors characteristic of different pore structures. SBA-15 exhibits a typical type IV isotherm with a hysteresis loop at $P/P_0 = 0.3–0.7$, confirming its mesoporous nature and ordered pore structure. Beta zeolite displays a type I isotherm with minimal hysteresis, characteristic of microporous materials. The mechanical mixture Beta/SBA-15 and core–shell Beta@SBA-15 both show composite isotherms combining features of both parent materials, indicating the coexistence of micro and mesoporous structures. The textural analysis reveals significant differences in pore structure distribution. SBA-15 demonstrates the highest external surface area (529 m^2 g^{-1}) and mesopore volume (0.587 cm^3 g^{-1}), with a narrow pore size distribution centered at around 6 nm. Beta zeolite exhibits predominantly microporous character with high micropore surface area (579 m^2 g^{-1}) and micropore volume (0.232 cm^3 g^{-1}), but minimal mesopore content (0.046 cm^3 g^{-1}). The mechanical mixture Beta/SBA-15 shows intermediate values representing simple additive effects of the individual components. Notably, Beta@SBA-15 achieves the highest BET surface area (736 m^2 g^{-1}) among all samples while maintaining substantial micropore surface area (551 m^2 g^{-1}) and moderate mesopore volume (0.225 cm^3 g^{-1}). This enhanced surface area in the core–shell structure, compared to both parent materials and the mechanical mixture, suggests synergistic effects arising from the intimate integration of Beta nanocrystals within the SBA-15 framework, creating additional accessible surface area at the core–shell interface while preserving the inherent porosity of both components.

Acidity evaluation using NH_3-TPD was performed with quantitative results and desorption profiles presented in Table 1 and Fig. 4, respectively. All samples exhibited two desorption peaks: a low-temperature peak (100–250 °C) corresponding to weak acid sites and a high-temperature peak (350–550 °C) attributed to strong acid sites. The acidity distribution inversely

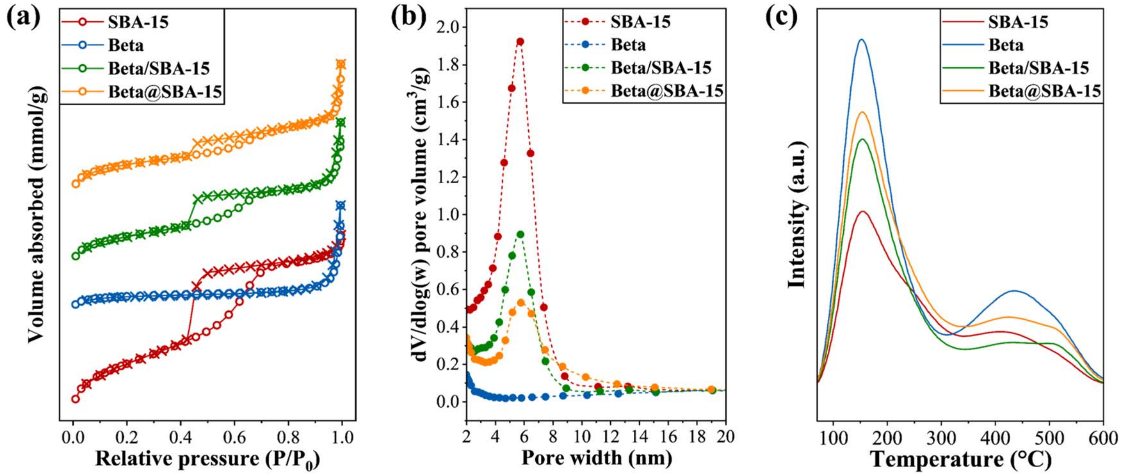

Fig. 4 (a) N_2 adsorption–desorption isotherms, (b) pore size distribution, and (c) NH_3-TPD profiles of synthesized zeolites.

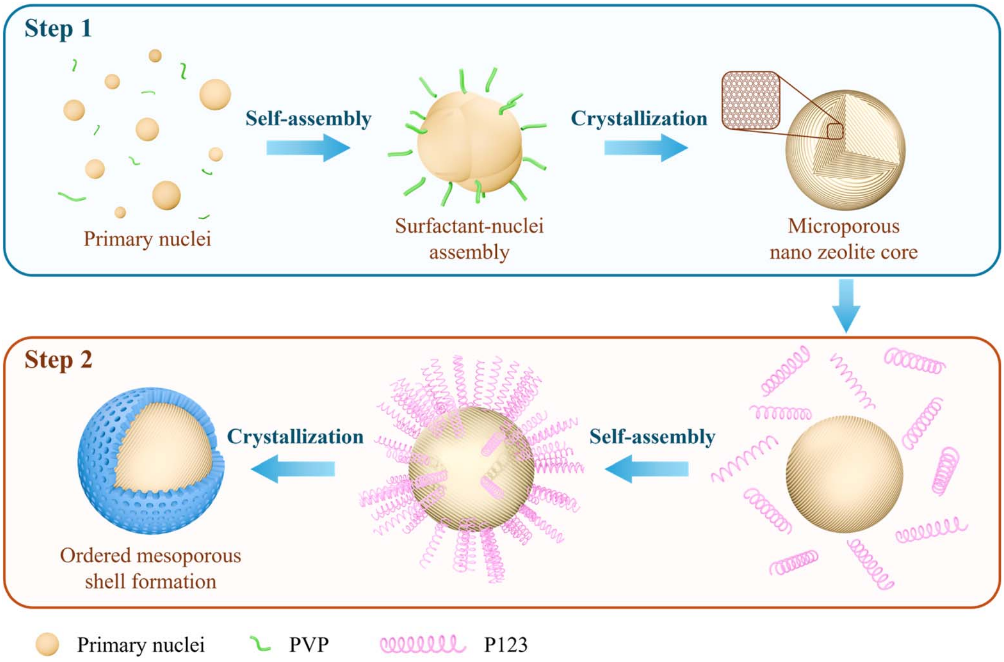

Fig. 5 Illustration of two-step crystallization process.

correlated with Si/Al ratios, with materials of higher aluminum content demonstrating greater acid site densities. Beta zeolite showed the highest total acid amount (1.537 mmol g^{-1}) and strong acid content (0.451 mmol g^{-1}), consistent with its lowest Si/Al ratio. SBA-15, with its purely siliceous composition, displayed minimal acidity (0.937 mmol g^{-1} total, 0.322 mmol g^{-1} strong). The mechanical mixture Beta/SBA-15 and core–shell Beta@SBA-15 revealed intermediate acidity values (1.093 and 1.183 mmol g^{-1} total, respectively), with Beta@SBA-15 exhibiting slightly higher acid content due to its lower Si/Al ratio.

The formation of the Beta@SBA-15 core–shell architecture involves a two-step crystallization process as illustrated in Fig. 5. Nano-sized Beta zeolite crystals are first synthesized *via* microwave crystallization using polyvinylpyrrolidone (PVP) as a crystal growth modifier. PVP coordinates with primary silica-alumina nuclei, forming surfactant-nuclei assemblies that inhibit particle aggregation and yield microporous nano zeolite cores of approximately 100 nm. In the second step, these pre-synthesized Beta nanoparticles serve as nucleation sites for mesoporous shell formation. The copolymer P123 adsorbs onto Beta particle surfaces through electrostatic and hydrogen bonding interactions, organizing silica species into micelle arrays that direct self-assembly. Microwave heating induces condensation of silica precursors around P123, resulting in the formation of a hexagonal mesoporous SBA-15 structure that uniformly encapsulates the Beta core with the assistance of $MgSO_4$. This stepwise approach achieves intimate integration of the microporous catalytic core with the ordered mesoporous transport shell, as confirmed by X-ray diffraction, transmission electron microscopy, and nitrogen physisorption analysis. The resulting hierarchical architecture enhances acid site accessibility within the Beta core while maintaining efficient mass transfer through the SBA-15 shell, thereby improving catalytic performance in supercritical hydrocarbon cracking.

3.2. Catalytic evaluation

The catalytic performance of synthesized zeolites was evaluated through *n*-decane cracking under supercritical conditions at temperatures ranging from 400–600 °C, with conversion results demonstrating distinct activity patterns correlating with catalyst acidity and pore structure characteristics (Fig. 6). SBA-15 exhibits the lowest conversion across the entire temperature range, increasing from 1.53% at 400 °C to 25.58% at 600 °C, reflecting its purely siliceous composition with minimal acid sites for catalytic cracking reactions. In contrast, Beta zeolite demonstrates the highest catalytic activity, achieving conversions from 5.36% at 400 °C to 46.61% at 600 °C. The mechanical mixture Beta/SBA-15 shows intermediate performance with conversions ranging from 2.85% to 36.13% across the temperature range, representing essentially additive effects of the individual components without synergistic enhancement. The core–shell Beta@SBA-15 catalyst exhibits remarkable performance, achieving conversions of 4.34% at 400 °C and 41.23% at 600 °C. Notably, the conversion at 600 °C corresponds to 88.5% of Beta's conversion (46.61%) despite Beta@SBA-15 possessing only 77.0% of Beta's total acidity (1.183 *vs.* 1.537 mmol g^{-1}). This discrepancy indicates enhanced acid site utilization efficiency in the core–shell structure. The hierarchical pore architecture enables improved reactant accessibility to acid sites within the Beta core, while the mesoporous SBA-15 shell facilitates efficient mass transfer. Consequently, the core–shell structure optimizes active site utilization, demonstrating significant advantages over conventional microporous catalysts and physical mixtures.

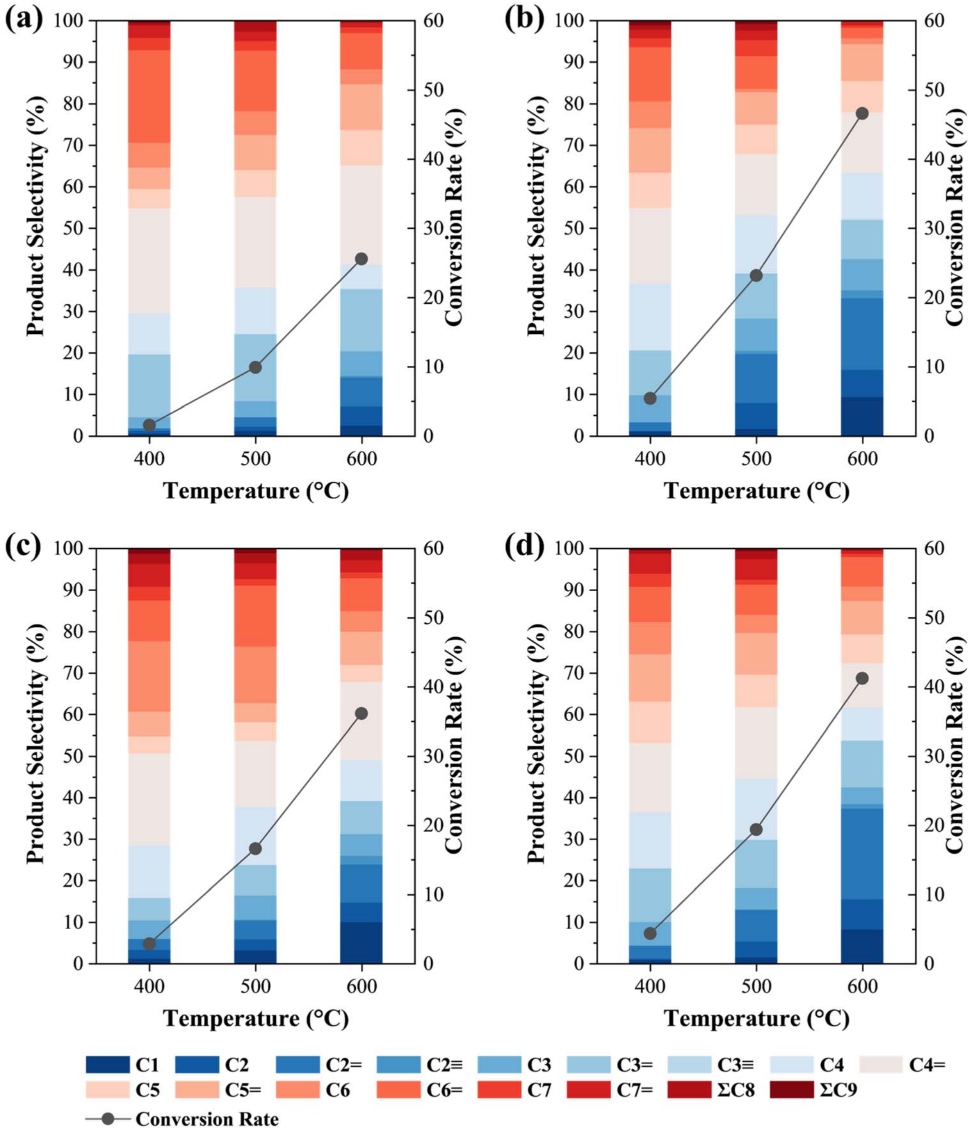

Fig. 6 Product distribution (bars) and *n*-decane conversion (lines) over SBA-15 (a), Beta (b), Beta/SBA-15 (c), and Beta@SBA-15 (d) zeolites at different temperatures.

To assess acid site utilization efficiency across catalyst architectures, conversion rates were normalized by total acidity. At 400 °C, Beta and Beta@SBA-15 exhibited comparable normalized conversions, indicating that the core–shell structure preserves Beta's catalytic effectiveness. As temperature increased, Beta@SBA-15 progressively outperformed Beta, achieving 16.37% and 34.85% per mmol acid at 500 °C and 600 °C, compared to Beta's 15.08% and 30.33%, respectively. This temperature-dependent enhancement reflects the superior mass transfer characteristics of the hierarchical pore network, which becomes increasingly advantageous under more severe reaction conditions. The comparison between Beta/SBA-15 and Beta revealed the importance of introduced mesoporous. While the mechanical mixture showed lower normalized conversion than Beta at 400 °C, it surpassed Beta's performance at elevated temperatures. This demonstrates that ordered mesoporous channels facilitate enhanced reactant accessibility and product evacuation under high-temperature conditions, enhancing the utilization of acid sites that would otherwise be constrained by pore blockage or mass transfer limitations in purely microporous frameworks (Table 2).

Table 2 Acidity-normalized conversion over different zeolites

Catalyst	Total acidity A_c (mmol g^{-1})	Normalized conversion (% per mmol acid)		
		400 °C	500 °C	600 °C
SBA-15	0.937	1.63	10.51	27.30
Beta	1.537	3.49	15.08	30.33
Beta/SBA-15	1.093	2.61	15.17	33.06
Beta@SBA-15	1.183	3.67	16.37	34.85

As shown in Fig. 6, Beta and Beta@SBA-15 catalysts demonstrate significantly higher yields of light hydrocarbons, indicating more extensive cracking reactions and deeper conversion of the *n*-decane feedstock compared to SBA-15 and the mechanical mixture. The Beta@SBA-15 core–shell catalyst maintains this deep cracking capability while benefiting from the hierarchical pore structure that enables efficient removal of primary cracking products before they undergo undesirable secondary reactions or contribute to coke formation. The mesoporous SBA-15 shell serves as molecular highways that facilitate rapid diffusion of both reactants and products, preventing the accumulation of intermediate species within the microporous Beta core that could otherwise lead to pore blockage or reduced selectivity toward desired light hydrocarbons. This structural advantage allows Beta@SBA-15 to achieve comparable deep cracking performance to pure Beta while maintaining better mass transfer characteristics that support sustained catalytic activity.

Quantitative analysis of product selectivity reveals the superior performance of the core–shell architecture in promoting light hydrocarbon formation. As shown in Fig. 7, all catalysts demonstrate increasing selectivity toward C_1–C_4 products with rising temperature, with Beta achieving the highest light hydrocarbon selectivity of 78.0% at 600 °C compared to 65.1% for SBA-15. The Beta@SBA-15 core–shell catalyst exhibits enhanced selectivity toward light hydrocarbons (72.4% at 600 °C) compared to the mechanical mixture Beta/SBA-15 (67.8%), demonstrating structural advantages beyond simple mixture effects. At moderate temperatures at 500 °C, Beta@SBA-15 outperforms the physical mixture by 8.1 percentage points, indicating that the integrated core–shell design facilitates more efficient cracking processes. The enhanced selectivity in Beta@SBA-15 stems from the optimized mass transfer characteristics provided by the hierarchical pore structure, where the mesoporous SBA-15 shell enables rapid evacuation of primary cracking products from the microporous Beta core before they undergo secondary reactions that typically favor heavier product formation. This efficient product removal prevents the accumulation of intermediate species within confined micropores, reducing the likelihood of consecutive reactions that would otherwise convert light hydrocarbons back to heavier fractions. Furthermore, the improved diffusion kinetics in the core–shell structure minimize residence time effects that often lead to product distribution broadening in conventional catalysts, thereby maintaining high selectivity toward the light hydrocarbon products while preserving the inherent cracking activity of the Beta zeolite framework.

3.3. Kinetic study

Apparent activation energies for *n*-decane cracking over the synthesized catalysts were determined using first-order reaction kinetics, a commonly employed assumption for fixed-bed reactor studies of heterogeneous catalysts.[24,33,34] The reaction rate constant k_T and apparent activation energy E_a were calculated using acid site-normalized methodology as represented by eqn (3) and (4), which provides a more accurate representation of intrinsic catalytic performance by accounting for the reaction occurring primarily at acid sites rather than conventional mass-based calculations.

$$\ln k_T = -\frac{E_a}{RT} + \ln A \tag{3}$$

$$k_T = \frac{F_{C_{10}H_{22}}}{WA_c} \times \left[-\ln\left(1 - X_{C_{10}H_{22}}\right)\right] \tag{4}$$

where k_T represents the reaction rate constant at specific temperature, $F_{C_{10}H_{22}}$ is the flow rate of *n*-decane, W denotes the

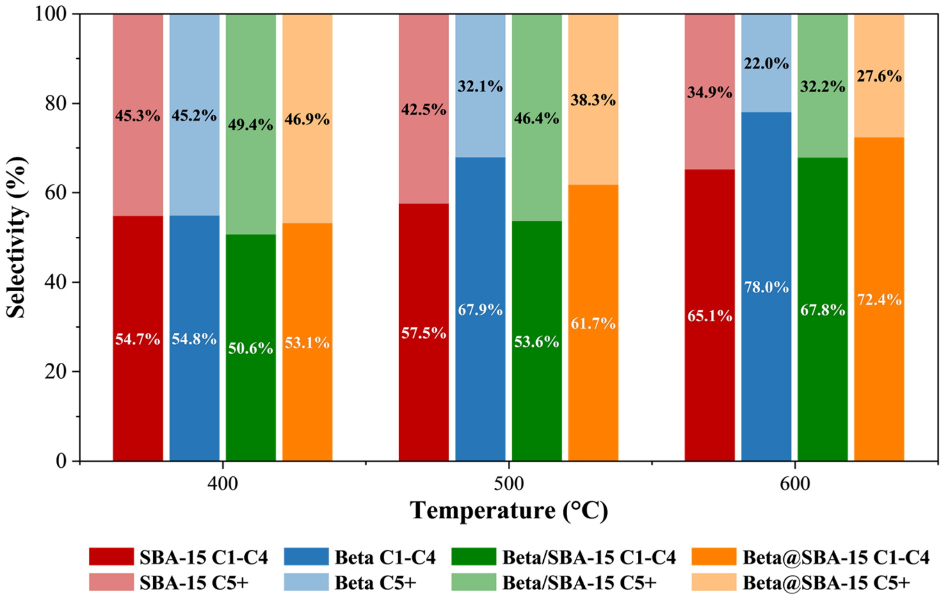

Fig. 7 Selectivity toward light (C_1–C_4) and heavy (C_{5+}) hydrocarbons of synthesized zeolites.

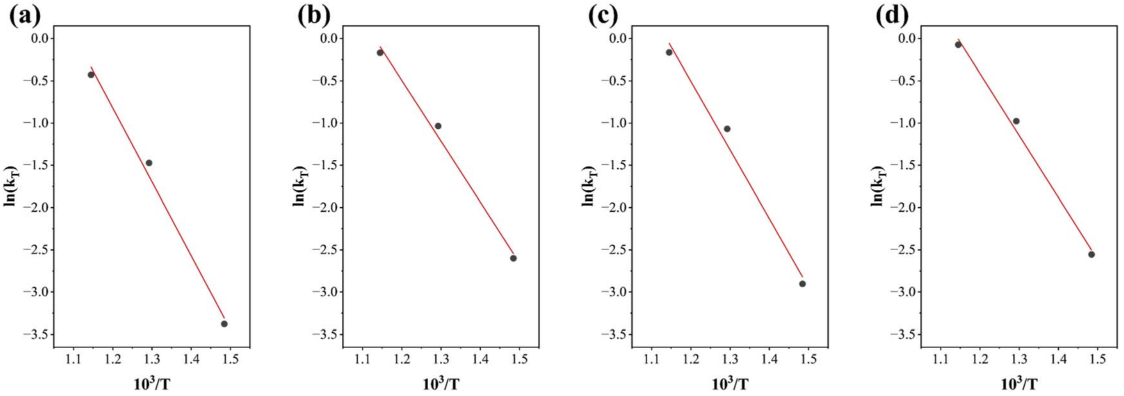

Fig. 8 Determination of apparent activation energy for *n*-decane cracking using SBA-15 (a), Beta (b), Beta/SBA-15 (c), and Beta@SBA-15 (d) zeolites *via* Arrhenius plots.

catalyst mass, A_c represents the total acidity of the catalyst, and $X_{C_{10}H_{22}}$ stands for the conversion rate of *n*-decane.

The apparent activation energies derived from Arrhenius plots (Fig. 8) demonstrate distinct kinetic behaviors correlating with catalyst acidity and structural characteristics. As shown in Table 3, SBA-15 exhibits the highest activation energy as 72.6 kJ mol^{-1}, reflecting its limited acid site density and weaker acidic strength that necessitate higher energy input to initiate reactions. In contrast, Beta zeolite demonstrates the lowest activation energy as 59.8 kJ mol^{-1}, consistent with its abundant strong acid sites that effectively reduce the energy barrier for cracking reactions. The mechanical mixture Beta/SBA-15 shows an intermediate activation energy, representing essentially weighted average effects of the individual components without synergistic enhancement. Notably, Beta@SBA-15 achieves an activation energy of 61.0 kJ mol^{-1}, remarkably close to Beta zeolite, indicating that the core–shell architecture successfully preserves the intrinsic catalytic activity of the Beta framework. This similarity in activation energies between Beta and Beta@SBA-15 confirms that the SBA-15 shell does not introduce additional kinetic barriers but rather maintains the accessibility of active sites within the Beta core while providing enhanced mass transfer properties. The correlation coefficients validate the applicability of first-order kinetics for describing *n*-decane cracking over these catalyst systems.

3.4. Evaluation of catalyst stability

Catalyst stability was assessed through time-on-stream experiments at 650 °C and 3.5 MPa over 15 hours. Fig. 9a reveals distinct catalyst deactivation patterns, offering insight into their long-term performance under reaction conditions. SBA-15 exhibits the lowest initial conversion (24.56%) and maintains relatively stable performance with minimal deactivation, declining to 17.42% after 15 hours. This behavior reflects its limited acidic sites and consequent low catalytic activity. In contrast, Beta zeolite demonstrates the highest initial conversion (45.25%) but undergoes significant deactivation, with conversion decreasing to 23.78%. The Beta/SBA-15 mixture shows intermediate initial activity (33.78%) but experiences similar deactivation, declining to 13.85% (59.00% relative decrease), suggesting that physical mixing does not enhance catalyst stability. After 11 hours, Beta/SBA-15 exhibits lower conversion than pure SBA-15, indicating that inadequate integration of microporous and mesoporous components compromises catalytic performance. This behavior reflects the disordered mass transfer environment in the physical mixture, where randomly distributed Beta particles disrupt the ordered mesoporous channels of SBA-15, creating tortuous diffusion pathways. Compared to the well-defined hexagonal mesoporous structure of pure SBA-15, this chaotic pore network intensifies diffusion limitations, resulting in substantial activity loss despite the presence of acidic sites from Beta. The comparison between Beta and Beta@SBA-15 reveals the critical advantage of the core–shell architecture. While Beta initially demonstrates higher conversion (45.25% *vs.* 41.87%) due to its greater accessible acid site concentration, this advantage rapidly diminishes as extensive coke formation occludes micropores and deactivates acid sites. In contrast, Beta@SBA-15 exhibits remarkable stability throughout the reaction period, maintaining 31.24% conversion after 15 hours (a relative decrease of only 25.39%). Notably, Beta@SBA-15 achieves the highest conversion among all catalysts after 15 hours, surpassing the initially superior Beta zeolite. The core–shell architecture enables sustained catalytic performance by facilitating efficient mass transfer through the mesoporous SBA-15 shell, mitigating coke accumulation that compromises conventional microporous catalysts. This combination of high activity and exceptional stability renders Beta@SBA-15 particularly promising for industrial applications requiring prolonged catalyst performance.

Table 3 Apparent activation energies and coefficients of determination for *n*-decane cracking over synthesized zeolites

Catalyst	SBA-15	Beta	Beta/SBA-15	Beta@SBA-15
E_a (kJ mol^{-1})	72.6	59.8	67.6	61.0
R^2	0.983	0.984	0.972	0.987

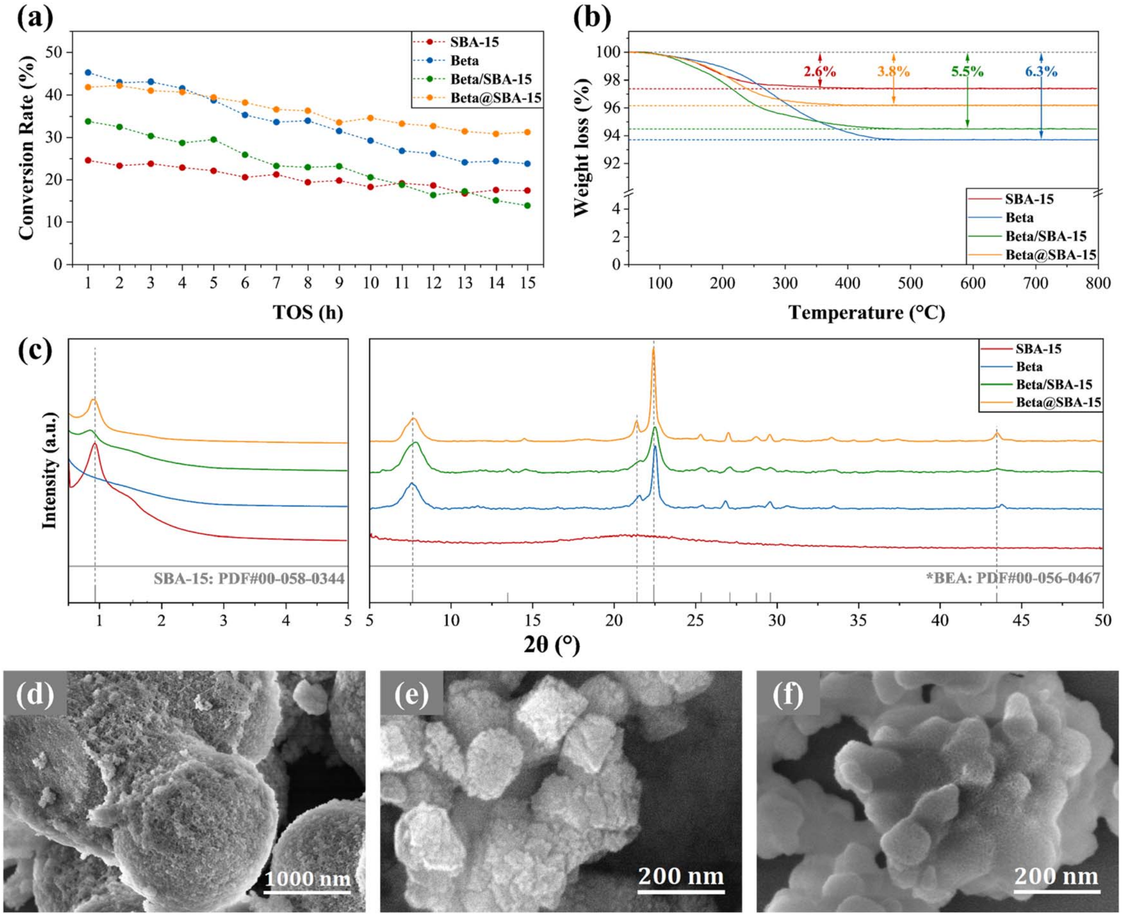

Fig. 9 (a) Time-on-stream performance of synthesized zeolites under 650 °C and 3.5 MPa, (b) TGA curves of spent zeolites, (c) XRD patterns of spent zeolites, and SEM images of spent SBA-15 (d), Beta (e), and Beta@SBA-15 (f) zeolites.

TGA results of the spent zeolites reveals significant differences in coke deposition, with weight losses of 2.6%, 6.3%, 5.5%, and 3.8% for SBA-15, Beta, Beta/SBA-15, and Beta@SBA-15, respectively (Fig. 9b). The minimal coke formation on SBA-15 reflects its purely siliceous nature with limited acidic sites for coke-forming reactions, while Beta zeolite exhibits the highest coke content due to the strong acidity and severe diffusion limitations within its microporous framework. The substantially reduced coking on Beta@SBA-15 compared to Beta and the mechanical mixture Beta/SBA-15 provides direct evidence for the mass transfer advantages of the core–shell architecture. In Beta zeolite, coke precursors generated at micropore-confined acid sites undergo extensive polymerization and condensation due to restricted diffusion, leading to the formation of bulky aromatic species that block pore channels. The weight loss profile extending beyond 400 °C confirms the presence of coke species requiring elevated temperatures for oxidative removal. In contrast, the core–shell structure of Beta@SBA-15 allows coke precursors to rapidly diffuse through the mesoporous SBA-15 shell before undergoing irreversible condensation reactions. This enhanced mass transfer is evidenced by the weight loss stabilization below 400 °C, indicating that carbonaceous deposits are predominantly located in the accessible mesoporous regions rather than trapped within micropores. The core–shell design thus effectively decouples the catalytic function from the diffusion limitation, enabling efficient removal of reaction intermediates and significantly mitigating coke formation while maintaining high catalytic activity.

XRD analysis of spent catalysts after TOS experiments reveals remarkable structural stability during reaction conditions (Fig. 9c). The comparison with fresh samples shows well-preserved characteristic diffraction patterns, indicating that the hexagonal mesoporous SBA-15 structure and *BEA zeolite framework maintain their crystallinity and structural integrity during harsh conditions. The Beta@SBA-15 catalyst maintains the structural features of both the Beta core and SBA-15 shell components, ensuring the integrity of the hierarchical pore architecture crucial for enhancing mass transfer. This stability provides a strong basis for potential catalyst regeneration.

SEM analysis of spent catalysts reveals morphological insights into coke deposition effects on surface structure. Comparison between fresh (Fig. 3a–c) and spent (Fig. 9d–f) samples demonstrates that overall particle size and macroscopic morphology remain well-preserved across all catalysts, indicating structural robustness under reaction conditions.

Surface textures, however, exhibit distinct changes depending on coke formation extent and location. SBA-15 shows minimal morphological alteration, with spherical particles maintaining smooth surfaces and ordered mesoporous channels. Conversely, Beta zeolite displays pronounced surface roughening, with initially well-defined cubic crystallites developing irregular surface features due to extensive coke accumulation on external surfaces and pore mouths. Beta@SBA-15 exhibits intermediate behavior, retaining spherical morphology while presenting slightly less defined surface textures. The preservation of particle integrity, coupled with surface modifications, suggests that deactivation occurs through reversible coke deposition rather than structural collapse, supporting potential catalyst regeneration through controlled oxidation procedures.

Textural analysis of spent catalysts reveals the impact of coke deposition on pore accessibility and structural integrity as shown in Table 4. Compared to fresh samples, all catalysts exhibit universal reductions in surface area and pore volume, with BET surface areas decreasing by 15–19% due to pore blockage by coke deposition. Micropore volume shows more severe reduction than mesopore volume, indicating preferential coke accumulation within confined micropores where mass transfer limitations impede coke precursor removal. This trend is most pronounced for Beta zeolite, with micropore volume decreasing from 0.232 to 0.172 $cm^3\ g^{-1}$ (25.9% reduction), while mesopore volume remains unchanged, confirming coke formation predominantly occurs at active sites within the microporous framework. Beta/SBA-15 experiences more dramatic micropore volume loss compared to Beta, suggesting the physical mixture configuration provides insufficient protection for the zeolitic component. In contrast, Beta@SBA-15 demonstrates more balanced textural degradation, with a 24.7% micropore volume reduction comparable to pure Beta but significantly better preservation of overall pore volume. The maintained micropore-to-mesopore ratio and superior total pore volume retention in Beta@SBA-15 indicate that the core–shell structure effectively mitigates pore blockage through enhanced mass transfer, enabling sustained accessibility to both microporous active sites and mesoporous transport channels.

Table 4 Textural properties of spent zeolites

	Surface area ($m^2\ g^{-1}$)			Pore volume ($cm^3\ g^{-1}$)		
Spent catalyst	S_{BET}	S_{micro}	S_{ext}	V_{total}	V_{micro}	V_{meso}
SBA-15	575	139	436	0.582	0.041	0.541
Beta	517	489	28	0.224	0.172	0.052
Beta/SBA-15	526	332	194	0.335	0.083	0.252
Beta@SBA-15	608	452	156	0.369	0.171	0.198

These stability results provide important context for interpreting the activation energy. Although Beta zeolite exhibits the lowest activation energy, this kinetic advantage does not translate into sustained catalytic performance owing to severe diffusion limitations within its purely microporous framework. In contrast, Beta@SBA-15 achieves comparable activation energy while demonstrating markedly superior stability, with only 25.39% conversion loss and 3.8 wt% coke deposition. This hierarchical core–shell architecture preserves the intrinsic catalytic activity of Beta zeolite while effectively mitigating transport constraints through the mesoporous shell. The superior catalytic activity and exceptional resistance to deactivation of Beta@SBA-15 demonstrate that optimal catalyst design for supercritical hydrocarbon cracking requires balancing intrinsic activity with long-term stability rather than solely minimizing activation barriers.

The superior performance of Beta@SBA-15 stems from synergistic interactions between the microporous Beta core and ordered mesoporous SBA-15 shell, establishing a hierarchical catalytic cascade as illustrated in Fig. 10. Large *n*-decane molecules initially undergo pre-cracking within mesoporous

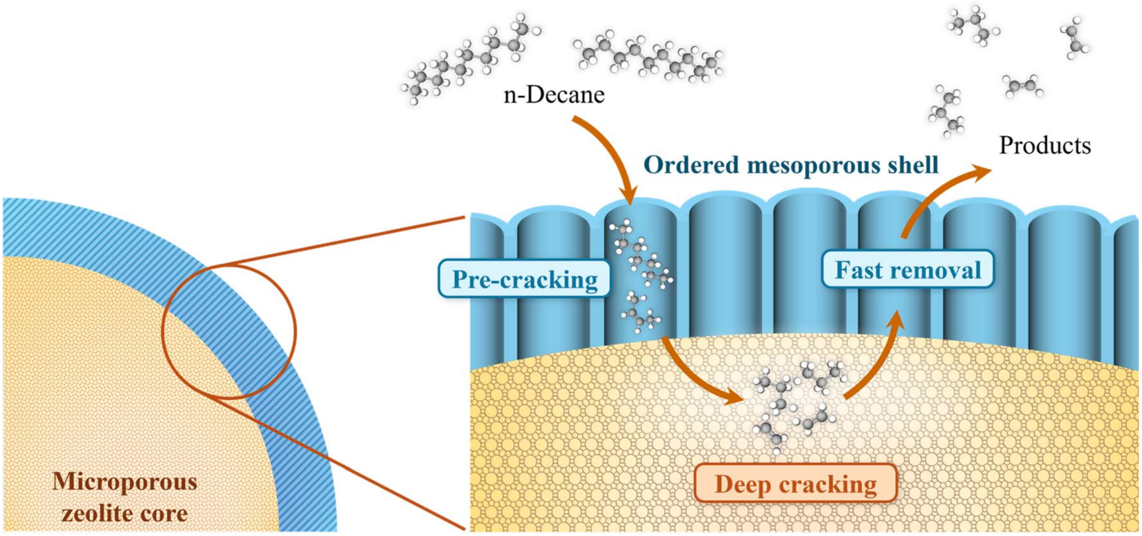

Fig. 10 Illustration of synergistic effect between microporous core and ordered mesoporous shell.

channels, generating smaller intermediates that subsequently diffuse through the mesoporous network to access concentrated acid sites in the microporous core for deep cracking. The ordered mesoporous shell functions as transport pathways, enabling rapid product evacuation and minimizing residence time near active sites, thereby suppressing secondary reactions and coke precursor formation. This spatial organization prevents catalytic activity from diffusion limitations by facilitating reactant pre-activation and mass transfer in the mesoporous shell while concentrating acid sites for selective hydrocarbon conversion in the microporous core, thereby achieving optimal conversion efficiency and long-term stability under extreme reaction conditions.

4. Conclusions

This study successfully synthesizes a hierarchical core–shell Beta@SBA-15 composite zeolite using microwave-surfactant prepared nano zeolite Beta as the core, demonstrating superior performance in supercritical *n*-decane catalytic cracking. Comprehensive characterization confirms the intimate integration of microporous Beta nanocrystals within ordered mesoporous SBA-15 shells, yielding a hierarchical architecture with an enhanced BET surface area of 736 $m^2 g^{-1}$ that surpasses both parent materials and mechanical mixtures. Despite containing 23.0% less total acidity than nano zeolite Beta, the core–shell Beta@SBA-15 achieves 88.5% of Beta's conversion at 600 ° C, exhibiting 14.9% higher acidity-normalized activity and demonstrating improved active site utilization efficiency. The core–shell structure preserves Beta's intrinsic catalytic activity, as demonstrated by similar apparent activation energies of nano zeolite Beta (61.0 and 59.8 kJ mol^{-1}, respectively), indicating that the SBA-15 shell does not introduce additional kinetic barriers but maintains the accessibility of active sites within the Beta core. This structural advantage maintains enhanced selectivity toward light hydrocarbons and enables remarkable deactivation resistance, with only 25.39% conversion loss over 15 hour time-on-stream tests compared to 47.45% for nano zeolite Beta. Thermogravimetric analysis reveals substantially reduced coke formation on Beta@SBA-15, attributed to the mesoporous shell facilitating rapid evacuation of coke precursors before condensation reactions occur. The synergistic integration of Beta's strong acidity and SBA-15's efficient mass transfer channels optimizes the spatial organization of catalytic sites and transport pathways, minimizing diffusion limitations while suppressing undesired consecutive reactions. These findings establish core–shell zeolite composites as a promising catalyst design strategy for hydrocarbon conversion processes under supercritical conditions, offering a generalizable approach to enhance both activity and stability through hierarchical zeolite utilization.

Author contributions

Hailong Ma: writing – original draft, visualization, validation, investigation, formal analysis, data curation. Hui Gao: writing – review & editing, supervision, resources, project administration, investigation, funding acquisition, conceptualization. Jieyin Ma: methodology, data curation. Jiajun Zhao: investigation, methodology, validation. Chen Zhang: investigation, validation, formal analysis. Dongsheng Wen: writing – review & editing, validation, supervision, project administration, methodology, funding acquisition, conceptualization.

Conflicts of interest

There are no conflicts to declare.

Data availability

All data generated or analyzed during this study (including characterization data, experimental results, and kinetic analysis) are included within the article through figures and tables.

Acknowledgements

This research is supported by the National Natural Science Foundation of China (No. 52472391), NSFC-DFG Mobility Programme (No. M-0368), and 111 Center (B18002).

References

1 S. Zhang, X. Li, J. Zuo, J. Qin, K. Cheng, Y. Feng and W. Bao, Research progress on active thermal protection for hypersonic vehicles, *Prog. Aero. Sci.*, 2020, **119**, 100646, DOI: 10.1016/j.paerosci.2020.100646.
2 D. Sziroczak and H. Smith, A review of design issues specific to hypersonic flight vehicles, *Prog. Aero. Sci.*, 2016, **84**, 1–28, DOI: 10.1016/j.paerosci.2016.04.001.
3 S. Dinda, K. Vuchuru, S. Konda and A. N. Uttaravalli, Heat Management in Supersonic/Hypersonic Vehicles Using Endothermic Fuel: Perspective and Challenges, *ACS Omega*, 2021, **6**, 26741–26755, DOI: 10.1021/acsomega.1c04218.
4 Y. Zhu, W. Peng, R. Xu and P. Jiang, Review on active thermal protection and its heat transfer for airbreathing hypersonic vehicles, *Chin. J. Aeronaut.*, 2018, **31**, 1929–1953, DOI: 10.1016/j.cja.2018.06.011.
5 O. Uyanna and H. Najafi, Thermal protection systems for space vehicles: A review on technology development, current challenges and future prospects, *Acta Astronaut.*, 2020, **176**, 341–356, DOI: 10.1016/j.actaastro.2020.06.047.
6 S. Luo, D. Xu, J. Song and J. Liu, A review of regenerative cooling technologies for scramjets, *Appl. Therm. Eng.*, 2021, **190**, 116754, DOI: 10.1016/j.applthermaleng.2021.116754.
7 G. Liu, X. Wang and X. Zhang, Pyrolytic depositions of hydrocarbon aviation fuels in regenerative cooling channels, *J. Anal. Appl. Pyrolysis*, 2013, **104**, 384–395, DOI: 10.1016/j.jaap.2013.06.007.
8 W. Ning, P. Yu and Z. Jin, Research status of active cooling of endothermic hydrocarbon fueled scramjet engine, *Proc. Inst. Mech. Eng., Part G*, 2012, **227**, 1780–1794, DOI: 10.1177/0954410012463642.
9 H. Li, H. Lan, Y. Sun, Q. Song, X. Wang, F. Li and W. Zhang, A review on pyrolysis and coking of liquid hydrocarbons in

heated pipe, *Appl. Energy*, 2025, **394**, 126159, DOI: 10.1016/j.apenergy.2025.126159.

10 B. Huang, U. Shrestha, R. J. Davis and H. K. Chelliah, Endothermic Pyrolysis of JP-10 with and without Zeolite Catalyst for Hypersonic Applications, *AIAA J.*, 2018, **56**, 1616–1626, DOI: 10.2514/1.J056432.

11 X. Li, H. Zhang, B. Liu, Q. Zhu, J. Wang and X. Li, Mo-promoted catalysts for supercritical n-decane cracking, *Appl. Therm. Eng.*, 2016, **102**, 1238–1240, DOI: 10.1016/j.applthermaleng.2016.04.009.

12 O. Rogala, K. A. Tarach, L. Lakiss, A. Kordek, V. Valtchev, J.-P. Gilson and K. Góra-Marek, Shaped zeolites Y for polypropylene cracking, *Appl. Catal. B Environ. Energy*, 2025, **365**, 124893, DOI: 10.1016/j.apcatb.2024.124893.

13 Z. Shen, C. Shi, F. Liu, W. Wang, M. Ai, Z. Huang, X. Zhang, L. Pan and J. J. Zou, Advances in Heterogeneous Catalysts for Lignin Hydrogenolysis, *Adv. Sci.*, 2024, **11**, e2306693, DOI: 10.1002/advs.202306693.

14 M. C. Shin, E. Magnone, B. J. Jeong, B. H. Jeong, X. Zhuang, J. Y. Hwang, J. I. Lee and J. H. Park, An experimental study of the endothermic catalytic cracking of hydrocarbon aviation fuels under extreme conditions, *J. Anal. Appl. Pyrolysis*, 2024, **181**, 106613, DOI: 10.1016/j.jaap.2024.106613.

15 Y. Ji, H. Yang and W. Yan, Strategies to Enhance the Catalytic Performance of ZSM-5 Zeolite in Hydrocarbon Cracking: A Review, *Catalysts*, 2017, **7**, 367, DOI: 10.3390/catal7120367.

16 X. Su, B. Liu, C. Feng and W. Wu, Rapid and low-cost synthesis of ZSM-5 zeolite nanosheet assemblies for conversion of methanol to gasoline, *Microporous Mesoporous Mater.*, 2022, **344**, 112215, DOI: 10.1016/j.micromeso.2022.112215.

17 L. Wei, H. Wang, Q. Dong, Y. Li and H. Xiang, A Review on the Research Progress of Zeolite Catalysts for Heavy Oil Cracking, *Catalysts*, 2025, **15**, 401, DOI: 10.3390/catal15040401.

18 J. Zhan, Y. Wang, T. He, L. Sheng, B. Wu, Q. Liu, M. Jia and Y. Zhang, Nonionic polymer and amino acid-assisted synthesis of ZSM-5 nanocrystals and their catalytic application in the alkylation of 2-methylnaphthalene, *Dalton Trans.*, 2024, **53**, 7384–7396, DOI: 10.1039/d4dt00096j.

19 M. Hartmann, M. Thommes and W. Schwieger, Hierarchically-Ordered Zeolites: A Critical Assessment, *Adv. Mater. Interfaces*, 2021, **8**, 2001841, DOI: 10.1002/admi.202001841.

20 S. Liu, Y. Tian, X. He, Y. Liu, C. Qiao and G. Liu, Moderation of textural properties in hierarchical ZSM-5 to enhance the yield of olefins in catalytic cracking of hydrocarbons, *Catal. Sci. Technol.*, 2023, **13**, 1119–1127, DOI: 10.1039/d2cy02137d.

21 A. Ishihara, M. Ninomiya, T. Hashimoto and H. Nasu, Catalytic cracking of C12-C32 hydrocarbons by hierarchical β- and Y-zeolite-containing mesoporous silica and silica-alumina using Curie point pyrolyzer, *J. Anal. Appl. Pyrolysis*, 2020, **150**, 104876, DOI: 10.1016/j.jaap.2020.104876.

22 L. Zhang, S. Qu, L. Wang, X. Zhang and G. Liu, Preparation and performance of hierarchical HZSM-5 coatings on stainless-steeled microchannels for catalytic cracking of hydrocarbons, *Catal. Today*, 2013, **216**, 64–70, DOI: 10.1016/j.cattod.2013.04.016.

23 B. Liu, Z. Wang, Q. Zhu, X. Li and J. Wang, Performance of Pt/ZrO2–TiO2–Al2O3 and coke deposition during methylcyclohexane catalytic cracking, *Fuel*, 2017, **200**, 387–394, DOI: 10.1016/j.fuel.2017.03.058.

24 H. Ma, H. Gao, H. Jin, K. Li and D. Wen, High-pressure catalytic dehydration of ethanol to ethylene over microwave-synthesized nanocrystalline zeolite β, *Mater. Today Chem.*, 2025, **46**, 102775, DOI: 10.1016/j.mtchem.2025.102775.

25 L. H. Chen, M. H. Sun, Z. Wang, W. Yang, Z. Xie and B. L. Su, Hierarchically Structured Zeolites: From Design to Application, *Chem. Rev.*, 2020, **120**, 11194–11294, DOI: 10.1021/acs.chemrev.0c00016.

26 P. Peng, X. H. Gao, Z. F. Yan and S. Mintova, Diffusion and catalyst efficiency in hierarchical zeolite catalysts, *Natl. Sci. Rev.*, 2020, **7**, 1726–1742, DOI: 10.1093/nsr/nwaa184.

27 R. Kumar Parsapur, A. M. Hengne, G. Melinte, O. Refa Koseoglu, R. P. Hodgkins, A. Bendjeriou-Sedjerari, Z. Lai and K. W. Huang, Post-Synthetic Ensembling Design of Hierarchically Ordered FAU-type Zeolite Frameworks for Vacuum Gas Oil Hydrocracking, *Angew. Chem.*, 2023, **136**, e202314217, DOI: 10.1002/ange.202314217.

28 Q. You, X. Wang, Y. Wu, C. Bi, X. Yang, M. Sun, J. Zhang, Q. Hao, H. Chen and X. Ma, Hierarchical Ti-beta with a three-dimensional ordered mesoporosity for catalytic epoxidation of bulky cyclic olefins, *New J. Chem.*, 2021, **45**, 10303–10314, DOI: 10.1039/d1nj00736j.

29 N. Masoumifard, R. Guillet-Nicolas and F. Kleitz, Synthesis of Engineered Zeolitic Materials: From Classical Zeolites to Hierarchical Core-Shell Materials, *Adv. Mater.*, 2018, **30**, e1704439, DOI: 10.1002/adma.201704439.

30 X. Qian, J. Du, B. Li, M. Si, Y. Yang, Y. Hu, G. Niu, Y. Zhang, H. Xu, B. Tu, Y. Tang and D. Zhao, Controllable fabrication of uniform core–shell structured zeolite@SBA-15 composites, *Chem. Sci.*, 2011, **2**, 2006, DOI: 10.1039/c1sc00250c.

31 J. Du, C. Shi, W. Wu, X. Bian, P. Chen, Q. Cui and Z. Cui, Synthesis of core-shell structured FAU/SBA-15 composite molecular sieves and their performance in catalytic cracking of polystyrene, *Sci. Technol. Adv. Mater.*, 2017, **18**, 939–949, DOI: 10.1080/14686996.2017.1396561.

32 L. Wang, Z. Diao, Y. Tian, Z. Xiong and G. Liu, Catalytic Cracking of Endothermic Hydrocarbon Fuels over Ordered Meso-HZSM-5 Zeolites with Al-MCM-41 Shells, *Energy Fuels*, 2016, **30**, 6977–6983, DOI: 10.1021/acs.energyfuels.6b01160.

33 O. B. Al-Ameri, M. Alzuhairi, Z. Shakor, E. Bailón-García, F. Carrasco-Marín and J. Amaro-Gahete, Kinetic and Thermodynamic Study of Vacuum Residue Cracking over Cerium-Modified Metakaolinite Catalyst, *Processes*, 2025, **13**, 3126, DOI: 10.3390/pr13103126.

34 A. Hart, M. Adam, J. P. Robinson, S. P. Rigby and J. Wood, Hydrogenation and Dehydrogenation of Tetralin and Naphthalene to Explore Heavy Oil Upgrading Using NiMo/Al2O3 and CoMo/Al2O3 Catalysts Heated with Steel Balls via Induction, *Catalysts*, 2020, **10**, 497, DOI: 10.3390/catal10050497.